Nickel-containing N-doped carbon as effective electrocatalysts for the reduction of CO_2 to CO in a continuous-flow electrolyzer

Nickel-containing N-doped carbon as effective electrocatalysts for the reduction of CO_2 to CO in a continuous-flow electrolyzer

Nick Daems[a,b,*,#], Bert De Mot[a,#], Daniel Choukroun[a], Kevin Van Daele[a,b] , Chen Li[c], Annick Hubin[d], Sara Bals[c], Jonas Hereijgers[a], Tom Breugelmans[a,b]

[a]*Applied Electrochemistry and Catalysis, UAntwerpen, Campus Drie Eiken, Universiteitsplein 1, 2610 Wilrijk, Belgium*

[b]*Separation & Conversion Technologies, Flemish Institute for Technological Research (VITO), Mol, Belgium*

[c]*Electron Microscopy for Materials Research (EMAT), University of Antwerp, 2020 Antwerp, Belgium*

[d]*Research Group Electrochemical and Surface Engineering, Vrije Universiteit Brussel, Pleinlaan 2, 1050 Brussels, Belgium*

[*]*Corresponding author, email: nick.daems@uantwerpen.be*

[#]*These authors contributed equally.*

Abstract: Nickel-containing N-doped carbons were synthesized for the electrochemical reduction of CO_2 to CO, which is a promising approach to reduce the atmospheric CO_2 levels and its negative impact on the environment. Unfortunately, poor performance (activity, selectivity and/or stability) is still a major hurdle for the economical implementation of this type of materials. The electrocatalysts were prepared through an easily up-scalable and easily tunable method based on the pyrolysis of Ni-containing N-doped carbons. Ni-N-AC-B1 synthesized with a high relative amount of nitrogen and nickel with respect to carbon, was identified as the most promising candidate for this reaction based on its partial CO current density (4.2 $mA.cm^{-2}$), its overpotential (0.57 V) and its Faradaic efficiency to CO (> 99%). This results in unprecedented values for the current density per g active sites (690 $A.g^{-1}$ active sites). Combined with its decent stability and its high performance in an actual electrolyzer setup, this makes it a promising candidate for the electrochemical reduction of CO_2 to CO on a larger scale. Finally, the evaluation of this kind of materials in a flow-cell setup has been limited and to the best of our knowledge never included an evaluation of several crucial parameters (e.g. electrolyte type, anode composition and membrane type) and is an essential investigation in the move towards up-scaling and ultimately industrial application of this technique. This study resulted in an optimal cell configuration, consisting of Pt as anode, Fumatech® as membrane and 1M $KHCO_3$ and 2M KOH as catholyte and anolyte, respectively. In conclusion, this research offers a unique combination of electrocatalyst development and reactor optimization.

Keywords: CO_2 electrolyzers, electrocatalysis, Ni-containing N-doped carbons, flow-cell

1. Introduction

Renewable energy sources can offer a solution for excessive emissions of greenhouse gases and to the expected decrease in availability of fossil fuels in the near future. Both problems would find a common solution if we were able to develop energy-efficient processes to convert CO_2 streams into fuels and useful chemical products, ensuring a positive economic and environmental balance. One possible strategy is to use H_2O and CO_2 as renewable

feedstock for production of fuels and chemicals (e.g. carbon monoxide, formic acid or methanol), employing excess electricity generated by renewable power sources (like wind or solar) to drive the reactions. In this aspect, the electrochemical CO_2 reduction is the most readily up scalable technology as it benefits from a relatively high efficiency and a product selectivity, which can be tuned towards a desired product by adapting the operating potential and/or the applied electrocatalyst.[1–4] This kind of system has three main benefits: (1) it can process CO_2 directly from (concentrated) waste industrial gas streams; (2) it offers a solution for the intermittent nature of renewable energy sources; and (3) it provides an alternative means of producing industrially valuable chemicals thereby decreasing the dependency on crude oils.[5–7]

Unfortunately, in order for this process to become a valuable alternative for current industrial chemical production processes, the performance of the applied electrocatalysts has to be further improved as they currently still lack sufficient activity, selectivity or stability. The main problems are the slow CO_2 reduction reaction kinetics, the competition with the hydrogen evolution reaction in aqueous media and the wide range of possible products (e.g. carbon monoxide, formic acid, methanol, methane, etc.), all of which result in poor energy efficiencies.[4,8,9] The most commonly applied CO_2 reduction electrocatalysts nowadays are metals and their complexes.[2,9] In terms of product selectivity, copper is the only pure metal that is capable of generating considerable amounts of hydrocarbons.[9–11] For this reason, Cu or Cu-derived materials have been widely investigated for this purpose since the first discovery by Hori *et al.*[11] As a result, it is now known that reaction conditions (e.g. electrolyte, pH, etc.[12]), applied potential[13] and metal properties (i.e. morphology, oxidation state, size and shape and presence of another metal[14]) have a significant impact on the electrochemical performance of Cu. Unfortunately, the formation of hydrocarbons is accompanied by high kinetic barriers as a consequence of the multiple electrons that need to be transferred, which ultimately results in rather high overpotentials and thus low energy efficiencies. The electroreduction of CO_2 to CO, on the other hand, only requires two protons and two electrons, making it a significantly faster process.[15] Furthermore, an additional advantage of producing CO is the fact that the otherwise unwanted hydrogen evolution reaction does not necessarily needs to be repressed. Indeed, by combining it with the electrochemically produced CO, syngas can be obtained, which is a valuable industrial feedstock that can be used in the Fischer-Tropsch process to generate synthetic fuels.

In order to make this an economically attractive alternative there is a critical need for an efficient and affordable electrocatalyst. Thus far, mainly Au[16,17] and Ag[18] were reported as the electrocatalyst of choice for the selective reduction of CO_2 to CO at low overpotentials. Unfortunately, due to their relatively low abundance in nature and either a low current density or insufficient stability, these electrocatalysts will not yield an economically viable production method, which is why earth-abundant electrocatalysts are required. In this respect, compound materials based on doped carbon materials including transition metals have recently gained attention.[4,15,19] The presence of a metal has been shown to be essential to reach sufficiently high performances (combination of activity, selectivity and stability) for the reduction of CO_2 to CO. Indeed, the presence of a metal strongly improves the activity and the production of CO compared to bare N-doped carbons, as was recently demonstrated by Varela *et al.*[4,15] Essential for their good performance are the single-atom metal sites coordinated with nitrogen (M-N_x). An interesting metal in this matter in terms of selectivity is nickel. On the one hand, in its pure metallic form, Ni mainly produces hydrogen[9] yet in a Ni-N_X configuration, on the other hand, it results in a selective reduction of CO_2 to CO.[19] This highlights the importance of the local electronic environment of the metal species for the

electrocatalyst's performance, in similarity with the impact of the support on the electrochemical performance of Sn for the CO_2 reduction, as was demonstrated by Zhao *et al.*[8]

While there is no doubt anymore regarding the excellent catalytic activity that Ni containing doped carbons display,[4,15,27,28,19–26] it is still not clear what is the impact of several essential parameters (e.g. electrolyte concentration, ink loading, metal content, synthesis method, cell configuration (electrolyte, anode, membrane), etc.) on their performance. This is the key issue of this paper. It will lead to new insights into how to improve their performance and can be used as guideline for future development of comparable materials but with a better overall performance.

Herein, we will thus further explore the application of Ni-containing N-doped porous activated carbon-based electrocatalysts (further referred to as Ni-N-C) for the electrochemical reduction of CO_2 to CO given their promising characteristics. Indeed, by combining two types of active sites (i.e. Ni-N_x and N sites inside the sp^2 carbon framework), both known to reduce CO_2 to CO, improved electrocatalysts are expected. On the one hand, the incorporation of nitrogen is expected to boost the activity as a consequence of the extra active sites that are included in the final material as compared to nitrogen-free carbon material. The latter stems from the disruption of the charge neutrality which is caused by the N incorporation, generating charged sites which most likely result in an easier adsorption and reduction of CO_2.[29] On the other hand, the incorporation of N also causes Ni to change configuration from metallic or oxide to a single atom Ni-N_X site, which has a better CO_2 reduction performance as already discovered in previous research. The latter might also have a beneficial effect on the overall stability of the material, as Ni leaching will be less likely to occur.

The reported work combines a thorough physicochemical characterization with an extensive electrochemical evaluation of the Ni-N-C materials. Together they lead to a better understanding of the material properties which leads to enhanced performance. Our results indicate that the incorporation of Ni into the final structure, yields materials with an enhanced performance (higher current densities and turnover frequency numbers to CO), which is in analogy with previous reports on similar materials.[15] Furthermore, by adapting the Ni loading and the moment in which it is incorporated, either during or after the synthesis of the doped carbon material, the correlation between the performance and the Ni-N_x content can be easily monitored. Finally, in order to investigate the viability of using Ni-N-C electrocatalysts in an actual electrolyzer, the best performing materials were also tested in an in-house designed CO_2 electrolyzer and its configuration optimized (e.g. membrane type, electrolyte composition and anode type). This study thus investigates if Ni-N-C electrocatalysts can be used as potential candidate towards up-scaling (and ultimately commercialization) of the electrochemical reduction of CO_2 to CO in attempt to reduce CO_2 emissions and generate alternative methods to obtain base chemicals.

2. Experimental

2.1 Materials

The following chemicals were used in this work: aniline (99.8% pure, Acros Organics), activated carbon Norit® SX1G (878 $m^2\ g^{-1}$, Norit Americas inc.), nickel(II)chloride hexahydrate (99.9%, Sigma Aldrich), nickel(II) nitrate hexahydrate (>99%, Sigma Aldrich), ammonium peroxydisulphate (98%, Acros Organics), potassium bicarbonate (99.7, Honeywell-Fluka), CO_2 (Grade 4.5, 99.995% Strombeek Ijsfabriek), sulphuric acid (>95%, Sigma Aldrich), hydrochloric acid (37% aqueous solution, Sigma Aldrich), nitric acid (70% aqueous solution,

Sigma Aldrich), Nafion® suspension (5 wt% in lower aliphatic alcohols and water, Sigma Aldrich), IrO_2 powder (99%, Alfa Aesar).

2.2 Synthesis of the electrocatalysts

Direct incorporation of Ni during synthesis of doped carbon

Ni-containing N-doped carbon materials were synthesized through previously reported procedures (Scheme 1).[29–31] First, impurities were removed from Norit® activated carbon (AC) by subjecting it to a 6M HCl aqueous solution for 24 h at room temperature. Next, 0.5 g of the purified carbon was immersed in 0.5M HCl at a temperature below 10°C. After 15 min, aniline (0.2 or 2.5 mL) was added and after an extra hour, ammonium peroxydisulphate (APS) $(NH_4)_2S_2O_8$, to promote aniline polymerization (1.2:1 molar ratio relative to aniline), and the nickel precursor, (1:1, 1:4 or 1:8 Ni:aniline molar ratio) both dissolved in 50 mL 0.5M HCl, were added to the resulting mixture. To allow complete polymerization this mixture was stirred for 24h while maintaining the temperature below 10°C. Afterwards, the solvent was evaporated using a Büchi rotavapor and further dried in an oven at 100°C overnight. Next, the powder was subjected to a first pyrolysis under Ar for 1 h at 900°C with a ramp of 3.3°C min^{-1}. Then, unstable (metal) species were removed by treating the solid with 0.5 M sulphuric acid for 8h in a reflux setup, which was followed by filtration, washing with deionized water and drying overnight at 100°C. Finally, the powder was subjected to a second pyrolysis step for 3h at 900°C. Five different sets of electrocatalysts (Scheme 1) were prepared and can be divided in two series: series A, in which a low amount of aniline, i.e. 0.2 mL, was used and series B, where a higher amount (2.5 mL) was utilized. For series B the metal to aniline ratio was also varied from 1:1 (A & B1) to 1:4 (B2) to 1:8 (B3). To give an example, Ni-N-AC-B2 was prepared using 0.5 g AC, 2.5 mL aniline and a metal to aniline ratio of 1:4. The APS/aniline ratio was kept constant for all materials, resulting in an increased APS/metal ratio from Ni-N-AC-B1 to –B3. As a reference, two metal-free materials were prepared: N-AC-pure-A and N-AC-pure-B, using 0.2 and 2.5 mL aniline, respectively and in analogy with the metal-containing electrocatalysts.

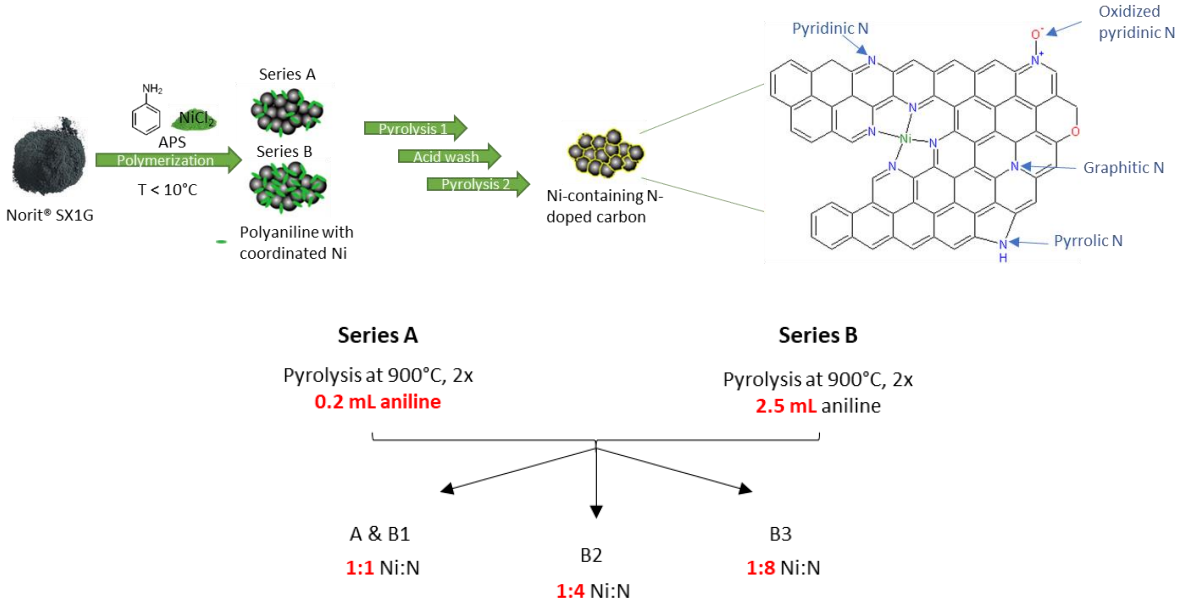

Scheme 1: Direct synthesis method of Ni-N-AC electrocatalysts and summary of the synthesis conditions for the different series of materials.

Post-synthesis incorporation of Ni into doped carbon

In an attempt to further increase the nickel loading and possibly alter the predominant Ni configuration of the prepared electrocatalysts an alternative method to incorporate nickel was also investigated (further referred to as Ni-N-AC-C). This method was inspired by a previously reported method in literature.[32] In short, 150 mg of the as-synthesized metal-free N-AC-pure-B sample was mixed with 100 mL DI water and sonicated for 30 min. Afterwards 185.8 mg $NiNO_3(H_2O)_6$ was added to achieve a final metal loading of 20 wt%. This mixture was stirred for 10 min, after which the pH was adjusted to 3.5 by adding some HNO_3. The mixture was then heated to 90°C. Once the desired temperature was achieved, 115 mg urea in 3 mL water was added and the mixture was stirred for 18h. Hydrolysis of urea causes a slow increase of the pH, which is a common approach to bring about the precipitation of metal salts onto a support.[32] In the next step, the mixture was cooled down, filtered, washed with water and dried in an oven at 100°C overnight. Finally, the residual material was reduced under the presence of hydrogen using the following temperature program: increase the temperature to 450°C at 10°C.min^{-1}, stay for 1h, further increase the temperature to 600°C at 20°C.min^{-1} and remain another hour at this temperature.

2.3 Physicochemical characterization

The different electrocatalysts were characterized with a set of techniques. Thermo-gravimetric analysis (TGA) was used to determine the Ni content, X-ray diffraction (XRD) to investigate the presence of Ni-based nanoparticles, N_2 physisorption to analyze sample porosity and surface area, X-ray photo-electron spectroscopy (XPS) to determine elemental composition and configuration, Raman to obtain information on the degree of graphitization and scanning transmission electron microscopy (STEM) and electron energy loss spectroscopy (EELS) to get a better idea on the material composition and configuration. Further information on the applied techniques can be found in the supporting information.

2.4 Electrochemical analysis

2.4.1 H-cell

All electrocatalytic measurements were carried out in a custom-made H-type cell equipped with a homemade cylindrical cathodic chamber, which is directly connected to an in-line gas chromatograph (Trace1300, Thermo Fischer Scientific). The liquid volume of the cathodic chamber was as low as 2.5 mL while the headspace volume was only ≈0.6 mL. Anodic and cathodic compartments were separated by a Nafion® 117 cation exchange membrane. As anode a rectangular Pt plate (0.5 cm², Meinsberg GmbH) was used. The reference electrode was a 4-mm Ag/AgCl (3M KCl, 0.210 vs. SHE, Metrohm) electrode. As a working electrode a catalyst-covered glassy carbon disk (0.28 cm²) was used. The working electrode was prepared by drop casting 14.14 µL of the catalyst ink onto the glassy carbon surface. The ink was prepared by dispersing 15.7 mg of electrocatalyst into 800µL MilliQ water, 150 µL isopropanol and 50 µL Nafion® solution (5wt%, Sigma Aldrich), resulting in 785 µg.cm^{-2} final loading.

The cathodic chamber was continuously purged with 1sccm CO_2 using a mass flow controller (GF-080, Brooks Instruments). We used 0.1 M or 0.5 M $KHCO_3$ both as anolyte and catholyte, but only the latter was purged with

CO_2. Electrochemical Impedance Spectroscopy (EIS) measurements were performed prior to each experiment to determine the uncompensated resistance R_u. The average value was taken and multiplied by a factor 0.85 for active ohmic drop correction. All potentials are reported versus the reversible hydrogen electrode (RHE). All measurements were performed using a potentiostat/galvanostat system (PARSTAT4000, Ametek® Princenton Applied Research) in duplicate (or triplicate) utilizing freshly deposited ink in each case. Initially, linear sweep voltammetry (LSV) measurements were performed at 5 $mV.s^{-1}$ between 0.3 and -1.1 V vs. RHE. These measurements were followed by chrono-amperometric measurements at different potentials (from -0.5 V to -1.1 V vs. RHE, with an increment of -0.1 V). Each potential was held for 30 minutes. After each 10 and 25 minutes the electrolysis products were separated using a micropacked column (ShinCarbon ST 100/120, 2 m, 1 mmID, Restek) and detected by a thermal conductivity detector (TCD) operating at 200°C. Liquid samples were analyzed for formic acid using high-performance liquid chromatography (Alliance 2695, Waters) and for methanol and ethanol using an off-line gas chromatograph, but no traces of these compounds were detected. To get an indication of the electrochemically active surface area the double-layer capacitance of all samples was determined by performing cyclic voltammetry experiments from 0.6 to 0.0 V vs. RHE at three different scanning rates (5, 10 and 20 $mV.s^{-1}$). The reported current densities were corrected for the difference in capacitance using the lowest value (20.2 mF cm^{-2} for Ni-N-C-B2) as base value.

2.4.2 Flow-cell

The continuous flow experiments were executed in a custom designed flow-by reactor set-up identical to the set-up described in our previous work[33] and is shown in Figure 1. CO_2 was fed at a rate of 100 $mL.min^{-1}$. The cathode was prepared by spray-painting the ink (25 mg catalyst, 1272 µL MQ water, 239 µL isopropanol and 80 µL 5 wt% Nafion® suspension) on top of the microporous layer of the GDE (Sigracet 39 BC, Fuel Cell Store). All the electrodes had an average catalyst loading of approximately 0.75 $mg.cm^{-2}$, which is very close to the loading during the H-cell experiments (0.785 $mg.cm^{-2}$).

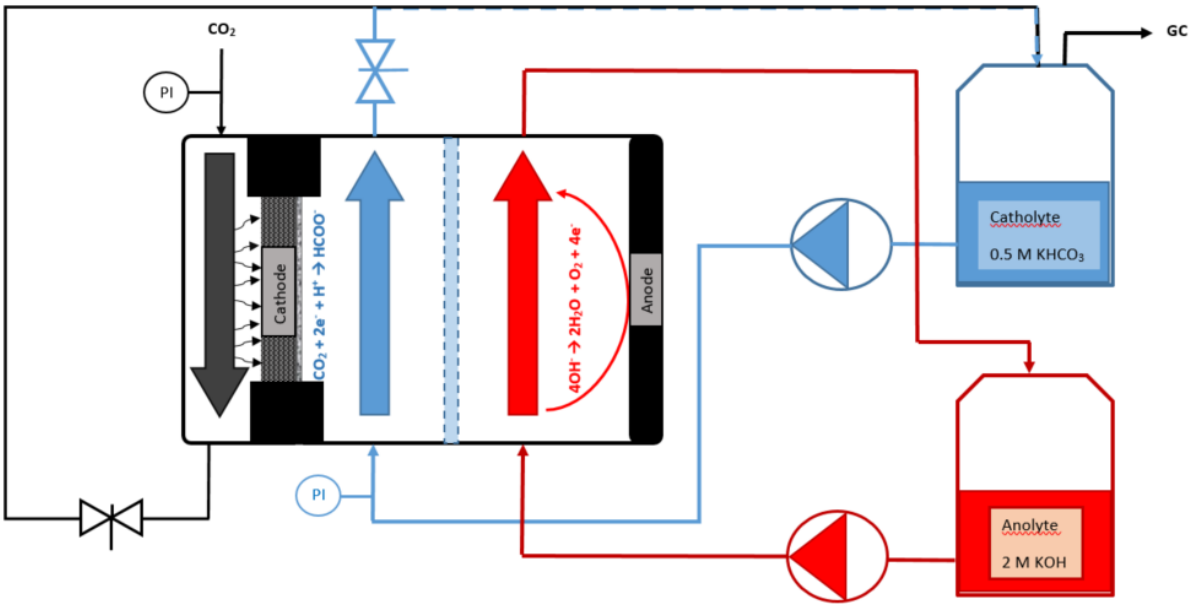

Figure 1. Schematic representation of the flow-by reactor setup used during the 24 h stability experiments. Catholyte flow (0.5 M $KHCO_3$) in blue, anolyte flow (2 M KOH) in red and the gas flow (CO_2) in black.

0.5 M aqueous $KHCO_3$ and 2 M aqueous KOH were chosen as catholyte and anolyte, respectively. During the 1 hour screening experiments the system was operated in single pass mode. A connection towards the GC was foreseen to allow gas sampling and analysis. For the 24 h stability experiments the system was operated in recirculation mode, Fig. 1. A Nafion® 117 cation exchange membrane was used to separate the catholyte and anolyte flow channel. In both system configurations the electrolyte flow rates were set at 10 ml/min.

A more detailed representation of the different reactor compartments is shown in Figure 2.

Figure 2. Detailed representation of the flow by reactor. Left to right: Aluminum back plate; Gas channel with turbulence promoter; Titanium cathode with GDE; Catholyte flow channel; Nafion® 117 membrane; Anolyte flow channel; Platinized titanium anode; Aluminum front plate with process connections; Rubber sealing.

To investigate the impact of cell configuration, several parameters were adapted in an attempt to achieve a more optimal composition as the original. To allow for a more optimal working of the cell in combination with the alkaline anolyte both an alternative membrane (Fumatech® FAA-3-20 (thickness: 20 µm and resistance: <2 Ω.cm²) or Selemion® AMV (thickness: 110 µm and resistance: ±3 Ω.cm²) and an alternative anode catalyst (IrO_2 commercial powder, spray-coated according a previously described procedure[34]) were investigated. Additionally, the impact of the anolyte and catholyte composition was also investigated ($KHCO_3$ or KOH on both sides vs. different catholyte and anolyte).

For both the batch and the flow cell the Faradaic efficiency of the gaseous product was calculated using the following equation (Eq. 1):

$$FE_i(\%) = Q_{exp,i}/Q_{total} = z.F.n_i /I.t \quad \text{(Eq.1)}$$

where $Q_{exp,i}$ is the amount of charge associated with the production of product i, also equal to the product of the number of exchanged electrons (z = 2 for CO), the Faraday constant (F, 96485 C mol^{-1}) and the number of moles of product (n_i), while Q_{total} is the total accumulated charge, which is equal to the collected current (I) multiplied by time (t).

3. Results and discussion

Ni-containing N-doped carbon electrocatalysts with different compositions (N content, Ni:N ratio) were prepared by two different methods: (1) by pyrolyzing Ni-coordinated polyaniline-covered activated carbons (Ni-N-AC-A & Ni-N-AC-B series) and (2) by post-doping N-doped carbons with Ni (Ni-N-AC-C). It is the first time that Ni is used in the synthesis of this specific type of Ni-N-AC electrocatalysts (method 1). In this study, the as-synthesized Ni-N-AC electrocatalysts were applied for the electrochemical reduction of CO_2 to CO.

By changing the composition of the initial synthesis mixture, we could tune the final composition and structure of the different electrocatalysts and get a better understanding of the most important parameters that govern the electrochemical performance. By performing a thorough physicochemical characterization, the most important material properties i.e. metal type, loading and configuration, N loading and configuration, surface area and degree of graphitization are determined for each material and linked with the electrochemical performance.

3.1 Physicochemical characterization

The characterization of the different materials started by determining the surface area and average pore size by means of N_2 physisorption (Table 1 and Fig. S1). The BET surface area of the different materials ranges from approx. 700 to 1100 $m^2.g^{-1}$, with a clear decrease in available surface area upon increasing the aniline and/or the metal content. Indeed, the series A catalysts, having the lowest aniline loading per amount activated carbon, exhibit the highest surface areas, while series C, combining a high aniline loading with a high metal content, has the lowest BET surface area. This could be expected as both the polyaniline layer and the non-porous metal species (oxides or hydroxides) are believed to cover/block the high surface area activated carbon.

Next, the surface composition and the overall metal content were determined for the different materials by means of XPS and TGA, respectively (Table 1). TGA analysis confirms that by increasing the amount of metal precursor while keeping the aniline amount constant, a higher overall metal content is achieved ([Ni] increases from Ni-N-AC-B3 to Ni-N-AC-B1). Furthermore, for the same Ni:aniline ratio (i.e. 1:1) but increasing the aniline loading, a higher amount of metal was maintained in the final material (Ni-N-AC-A vs. Ni-N-AC-B1). This is believed to have two main causes. First, the initial amount of Ni precursor that was present in Ni-N-AC-A (≈1g) is lower than that in Ni-N-AC-B1 (≈6g). Second, a higher initial aniline content (as is the case for Ni-N-AC-B1) is expected to allow for a larger fraction of the metal atoms to be retained. Indeed, the available literature indicates that Ni will mainly be present in a coordination with N-atoms doped into the carbon framework. However, no linear correlation could be found between the increase in initial metal content and the final incorporated metal content, which suggests that the number of N atoms is insufficient to bind all available metal species. This in turn will result in the presence of metal species other than those coordinated with N as also evidenced by XRD and XPS (*vide infra*). Ni-N-AC-C finally, has the highest overall metal content, which is believed to be a result of having the highest amount of Ni added per carbon content and of being produced by a different post-synthesis addition method. As for the XPS results, a lower almost constant Ni content was observed for the three different B series electrocatalysts, while no Ni and a higher Ni content was detected for Ni-N-AC-A and Ni-N-AC-C, respectively. When only looking at the different series A vs. B vs. C these results are in accordance with the values obtained from TGA and the ones that were expected based on the initial synthesis mixture. Furthermore, since

XPS is a surface sensitive technique it is believed that the lower values with respect to TGA are the consequence of the presence of one or several layers of graphitic carbon on a large fraction of the metal particles for the materials synthesized with the in-situ Ni doping. For series C, on the other hand, the Ni XPS content is larger than the TGA content and this is most likely caused by the fact that Ni is added after synthesizing the N-doped carbon mainly limiting its presence to the surface layers. Finally, also for XPS the absence of a correlation between Ni:aniline ratio and the detected metal content is again linked to a lack of available N atoms. As for the N content, it appears that it increases with the initial aniline content but decreases with the metal loading. While the former is straightforward, the latter might find its explanation when looking at the standard reduction potential (E°) of Ni, which is negative (-0.25 V_{SHE}) meaning nickel will more likely act as a reductant and inhibit the working of the oxidant (APS) thus slowing down or inhibiting the polymerization reaction. This will ultimately result in a lower amount of N atoms that becomes incorporated in the final material.[29]

Table 1. BET surface area, average pore size, surface composition and overall metal content of the different electrocatalysts.

Sample	S_{BET} ($m^2.g^{-1}$)	Pore size (nm)	Wt% C (XPS)	Wt% O (XPS)	Wt% N (XPS)	Wt% Ni (XPS)	Wt% Ni (TGA)
N-AC-pure-A	1060	2.8	94	2.4	2.5	0	0
N-AC-pure-B	763	3.4	86	2.8	7.2	0	0
Ni-N-AC-A	1050	3.3	96	1.6	1.2	0	2.6
Ni-N-AC-B1	772	2.0	92	2.6	1.6	1.3	4.4
Ni-N-AC-B2	824	3.7	94	1.6	2.5	1.2	3.9
Ni-N-AC-B3	924	1.9	90	3.0	3.7	1.2	2.4
Ni-N-AC-C	695	2.0	44	19	2.5	34	11

To analyze the different electrocatalysts for the presence of crystalline phases and identify them, XRD was used. For all the electrocatalysts, the formation of a graphitic carbon framework (although with low degree of crystallinity) was evidenced by the presence of two peaks at around $2\theta = 26°$ and 44° (Fig. S2).[35] This observation will be further confirmed by Raman spectroscopy (*vide infra*). Besides the presence of a graphitic carbon framework, two other species can be distinguished in the XRD diffractograms (Fig. S2), namely $Ni(OH)_2$, which is present in all Ni-containing samples except for Ni-N-AC-C, whose diffractogram is dominated by metallic Ni.[36–38] These results are confirmed by deconvoluting the Ni 2p XPS spectra of the respective samples as will be discussed later on. It is believed that the deviant Ni configuration of Ni-N-AC-C as compared to the other Ni electrocatalysts is a consequence of the difference in synthesis method. Indeed, the incorporation of Ni post-synthesis, which is followed by a reduction under hydrogen is probably more likely to result in the formation of metallic nickel rather than yielding nickel hydroxides.

Raman spectra were recorded to gain insight in the degree of graphitization (linked with material conductivity) and the number of defects in the prepared electrocatalysts (Fig. 3 and Table 2). Two distinctive peaks can be distinguished in the overall Raman spectra of all materials, namely the G-band, located at 1590-1600 cm^{-1} and characteristic for the presence of graphitic carbon and the D-band, located at 1350 cm^{-1} and characteristic for the presence of defects and disordered structures inside the sp^2 domain.[39] Upon deconvolution, two additional peaks appear at 1200 and 1500 cm^{-1}. The former is attributed to C atoms outside the ideal sp^2 plane and the latter, also called the A-band, is assigned to the presence of heteroatoms (in this case N) inside the graphitic framework.[35]

The extent to which a graphitic carbon is formed is generally correlated with two parameters: the ratio of the area of the D over the G band (A_D/A_G), which is inversely proportional to the graphitic degree; and the full-width at half-maximum (FWHM) of the D-band, a higher value indicating a less graphitic material (Table 2).[30,39,40] Based on the available data, it could be concluded that the highest degree of graphitization was achieved with Ni-N-AC-A, followed by Ni-N-AC-B, N-AC-pure-A, Ni-N-AC-C and N-AC-pure-B. This is in accordance with our expectation based on the initial aniline and metal contents. Indeed, a higher initial aniline content results in a higher amount of N incorporated in the carbon structure (Table 1) and thus a lower degree of graphitization as the incorporation of N tends to disrupt the order (e.g. compare N-AC-pure-A with N-AC-pure-B). Additionally, since Ni is known as a good catalyst to promote graphitization,[41] it is only logic that the degree of graphitization increases with the incorporation of Ni (e.g. N-AC-pure-A vs. Ni-N-AC-A). Finally, although Ni-N-AC-C has the highest Ni content its degree of graphitization is comparable to that of N-AC-pure-B, which was expected as Ni was only added after the carbon framework was produced.

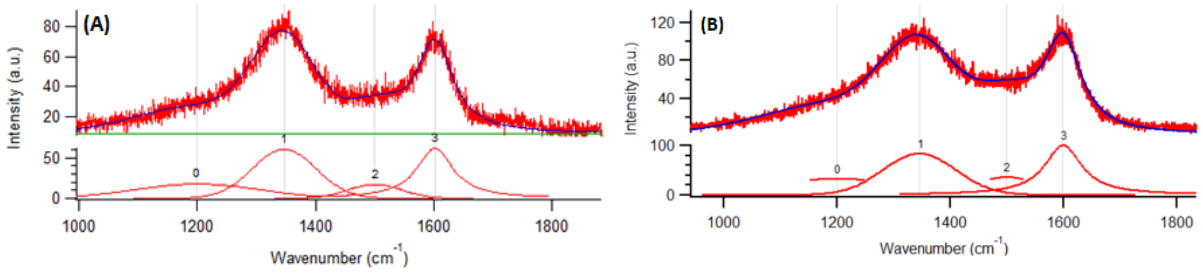

Figure 3. Deconvoluted Raman spectra of N-AC-pure-B (A) and Ni-N-AC-A (B).

Table 2. Summary of parameters related with degree of graphitization (Raman) and N configuration and percentage of surface Ni oxides (XPS).

Sample	A_D/A_G	FWHM (D-band)	Pyridinic N[a]	Pyrrolic N[a]	Graphitic N[a]	Oxidized pyridinic N[a]	Ni-N_x[a]	Wt% Ni in Ni-N_x[b]
N-AC-pure-A	1.05	128	32	4.1	53	11	/	/
N-AC-pure-B	1.12	130	33	4.4	53	10	/	/
Ni-N-AC-A	0.92	120	n.d.[c]	n.d.[c]	n.d.[c]	n.d.[c]	n.d.[c]	n.d.[c]
Ni-N-AC-B1	0.98	121	9.8	0.0	56	7.2	27	0.93
Ni-N-AC-B2	0.99	122	16	5.7	57	10	11	0.83
Ni-N-AC-B3	0.99	124	21	4.6	50	12	13	0.59
Ni-N-AC-C	1.11	129	15	0.0	64	9.6	11	3.49

[a]Obtained by deconvolution of high resolution XPS N1s spectra with Multipak.

[b]Obtained by deconvolution of high resolution XPS Ni2p spectra with Multipak. The remainder of Ni is present as metallic Ni or Ni oxide and/or hydroxide as determined by deconvolution.

[c]Not determined due to too low signal-to-noise ratio.

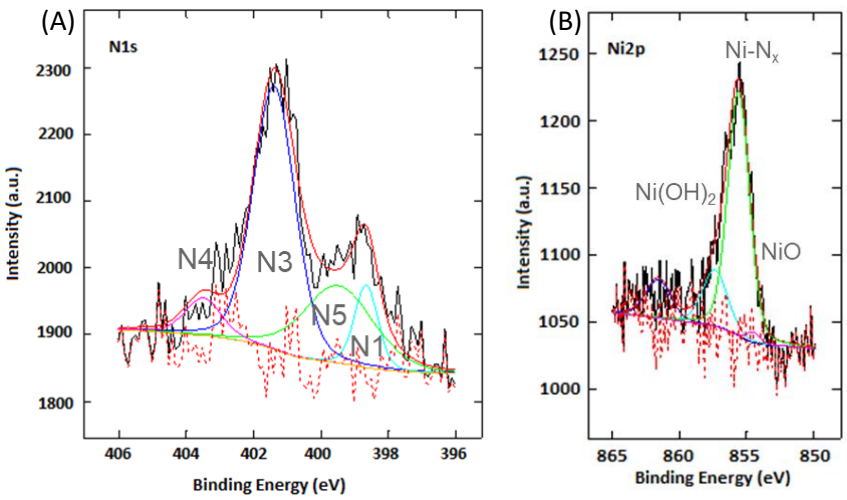

Figure 4. Deconvoluted XPS spectra of Ni-N-AC-B1: N1s (A) and Ni2p (B).

More detailed information on the surface chemical composition and configuration of the different elements at the surface can be obtained by deconvoluting the high resolution XPS spectra. Fitting the high-resolution N1s spectra (Fig. 4 and Fig. S3 to S6) revealed the presence of four or five different nitrogen species, namely, pyridinic N (N1, 398.6 eV), pyrrolic N (N2, 400.5 eV), graphitic N (N3, 401.5 eV), oxidized pyridinic N (N4, >403 eV) and most importantly nickel-coordinated Ni-N_x species (N5, 399.5 eV).[4,39] The latter are believed to be the most important sites for the electrochemical reduction of CO_2. All the N1s spectra are dominated by the graphitic nitrogen moiety (>50%), further evidencing the high degree of graphitization of these samples as was determined by Raman spectroscopy.[39] The difference between the metal-free electrocatalysts (N-AC-pure) and the Ni-containing samples (Ni-N-AC) is situated in the relative fractions of N1 and N5 species. The former (pyridinic N) being more abundant in the N-AC-pure materials and the latter for obvious reasons being only present in the Ni-containing material.[20,30,39] Additionally, the fraction of Ni-N_X moieties clearly increased from Ni-N-AC-B2 to Ni-N-AC-B1, which is as expected based on the relative Ni contents in the synthesis mixture. The relative content of Ni-N_x species for Ni-N-AC-C is much lower as expected based on the Ni loading and this has two possible explanations: (1) not enough N sites are available to coordinate all the Ni present in the sample (as also proven by the deconvolution of the Ni2p XPS spectra) and (2) post-doping the sample with Ni is a less efficient method to achieve the desired Ni-N_X moieties.

The presence of Ni-N_X moieties was further confirmed by deconvoluting the high resolution Ni $2p_{3/2}$ XPS spectra (Fig. 4 and Fig. S3 to S5), where the Ni-N_X species (855.3 eV[4,26]) are clearly the most dominant ones. The other peaks at 854.2 eV and 857.1 eV can be assigned to NiO and $Ni(OH)_2$, respectively.[42,43] The presence of the latter confirms the XRD spectra. For Ni-N-AC-C a fourth peak (852 eV) can be distinguished that is characteristic for the presence of metallic Ni, which is again in accordance with the XRD results. The remaining peak at ≈862 eV is the satellite peak.[42,43] The Ni $2p_{1/2}$ XPS spectra were removed from the deconvoluted graphs as their signal-to-noise ratio (see Fig. S7) was too low for most samples to allow an accurate deconvolution. Combining these results with the surface Ni content, it was determined that the Ni-N_X content increases from Ni-N-AC-B3 (0.59 wt%) to Ni-N-AC-B2 (0.83 wt%) to Ni-N-AC-B1 (0.93 wt%) to Ni-N-AC-C (3.49 wt%), as expected based on the relative compositions of the initial synthesis mixtures and the synthesis method. Indeed, incorporation of Ni

prior to the formation of the graphitic carbon framework will facilitate the formation of Ni-N_X moieties as compared to post-synthesis incorporation, which is the case for Ni-N-AC-C thus explaining its low Ni-N_X content. Indeed, only 10% of the available Ni is present as Ni-N_X while this amounts to more than 70% for Ni-N-AC-B1. In absolute amount however, Ni-N-AC-C does have the largest fraction of Ni-N_X species but this does not result in a better performance (*vide infra*) which means its performance is dominated by the other Ni species (e.g. metallic Ni, or Ni (hydr)oxides). When comparing the relative Ni-N_X contents as determined from the N 1s and from the Ni 2p XPS spectra, a discrepancy can be observed, e.g. Ni-N_X content is higher for Ni-N-AC-B3 than for Ni-N-AC-B2 according to the N 1s spectra while the opposite seems to be the case when looking at the Ni 2p spectra. This is believed to be a consequence of the closer proximity of the peaks in the N 1s spectra complicating the deconvolution. Indeed for the deconvolution of the N 1s spectra there are three different species that can be found at rather similar binding energies. The results of the deconvolution of the Ni 2p XPS spectra might be more trustworthy as they should be more accurate.

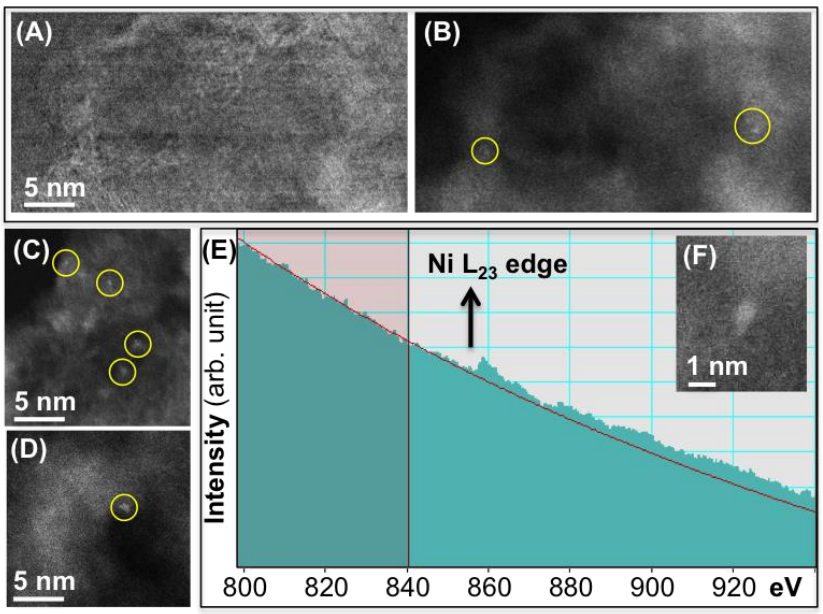

Figure 5. STEM-EELS showing single atom Ni on the doped carbon support (Ni-N-AC-B1). (A-B): simultaneous LAADF and HAADF images showing carbon fringes in (A) and heavy single atoms in (B). Heavy single atoms are marked by yellow circles. (C): HAADF image from another area again showing bright atoms, showing a representative morphology for the Ni-N-AC-B1 sample. (D): A bright spot slightly larger than a single atom, which is likely a cluster of only a few atoms. (E): EELS on such a tiny cluster of a few atoms as shown in (F) detects a clear Ni L_{23} edge confirming that the bright atoms are indeed Ni.

Finally, STEM high-angle dark-field (HAADF) imaging has been used to confirm the distribution of Ni and/or NiO_x in Ni-N-AC-B1 and Ni-N-AC-C, respectively. As the signal of the HAADF-STEM image is approximately proportional to the square of the atomic number Z, the Ni single atoms can be distinguished from the doped carbon framework in the HAADF images due to its higher Z number (28) as compared with carbon (6) and nitrogen (7). Fig. 5(A) and (B) are a set of low-angle annular dark-field (LAADF) and HAADF images recorded simultaneously from the same area. As the LAADF image collects partially the bright field signal, Fig. 5(A) shows clear fringes of the carbon support. Meanwhile the HAADF image in Fig. 5(B) shows a much stronger signal of certain heavier elements, as marked by yellow circles. Note there are two heavy atoms in the large circle on the right side of Fig.

5(B). Fig. 5(C) is a HAADF image from another area again showing the brighter atoms (marked by the yellow circles), which is also observed from many other areas proving this is a representative morphology throughout Ni-N-AC-B1. Occasionally a bright spot that is slightly larger than a single atom was detected as shown in Fig. 5(B). These are likely a cluster of only a few atoms, according to its tiny size (<1 nm). The EELS signal from one single bright atom is not strong enough to clearly identify the atom, however EELS on a cluster of a few atoms detects a clear Ni L_{23} edge proving that the detected bright atoms are indeed Ni, as shown in Fig. 5(E-F). These results thus agree well with the presence of Ni-N_X inside the material as already suggested based on the XPS data.[28,44]

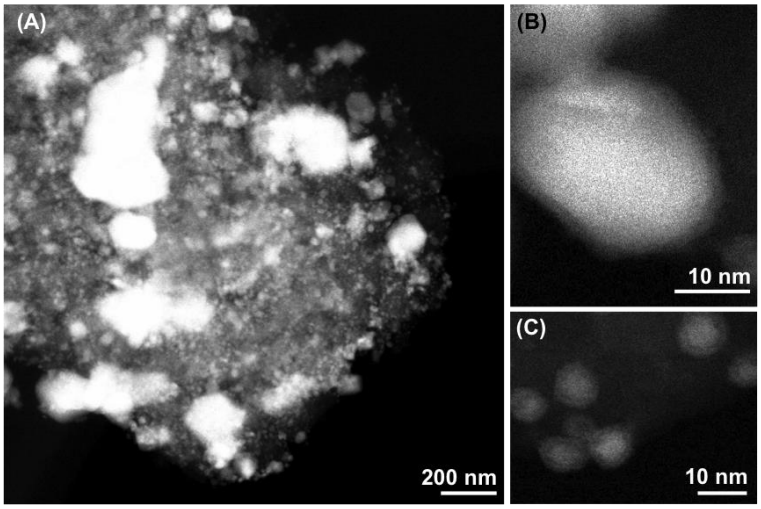

Figure 6. STEM-HAADF images show Ni oxides or hydroxides on the doped carbon support of Ni-N-AC-C. (A): the particles exhibit a diverse size distribution ranging from 8 to a few hundred nm. (B-C) HAADF images showing Ni particles with size from 20-30 and from 8-10 nm, respectively. Both have a weaker intensity for the shell, thus indicating the presence of lighter elements in this zone.

The morphology of Ni-N-AC-C however is quite different as was already expected based on the XPS and XRD data. Indeed a much larger fraction of nickel(hydr)oxide particles possibly hiding the presence of single Ni atoms was expected. This was clearly also confirmed by HAADF-STEM, as can be observed in Fig. 6(A), which shows Ni particles with a diverse size distribution ranging from 8 nm to a few hundred nm. The STEM-HAADF image in Fig. 6(B-C) show particles with sizes from 20-30 and from 8-10 nm, respectively. In both cases the particles exhibit a lighter intensity on the shells indicating the presence of light elements inside the shell, which based on the XPS results are likely oxygen atoms and confirm the presence of a large fraction of Ni(hydr)oxides in Ni-N-AC-C.

In conclusion, this combination of characterization techniques revealed the formation of a Ni-containing N-doped graphitic carbon with a dominant presence of nickel-single atom sites (Ni-N_X) for most Ni-N-AC samples, Ni-N-AC-C being an exception because of its different synthesis method.

3.2 Electrochemical analysis

3.2.1 Batch-cell

In order to obtain a meaningful comparison between the electrochemical performances of the different electrocatalysts, we normalized their activity (expressed in mA cm^{-2}) with respect to the double-layer capacitance of each electrode (Fig. S8 and Table S1) as this can be associated with the electrochemically active surface area (EASA).[3] The double layer capacitance was determined by plotting the difference in current density ($\Delta J = (J_{anodic} - J_{cathodic})/2$) at 0.3 V_{RHE} against the scan rate. ΔJ was acquired from cyclic voltammetry experiments in the potential range from 0.0 to 0.55 V_{RHE} in 0.1M aqueous $KHCO_3$. This results in a straight line whose slope was taken as a value for the capacitance. The lowest capacitance (here obtained with Ni-N-AC-B3) was set to unity (i.e. a roughness factor of 1) while the roughness factor of the other materials was calculated with respect to Ni-N-AC-B3 (see Table S1).

The first evaluation of the electrochemical performance of the different electrocatalysts was performed by linear sweep voltammetry (LSV, Fig. S9). By comparing the measurements obtained in the CO_2-saturated solution with those measured in the absence of CO_2 (Fig. S9), it is clear that the activity of Ni-N-AC-B1 originates from the CO_2 reduction as much lower currents were recorded in the absence of CO_2. The activity of the different materials can first be ranked based on the onset potential (determined as the potential where the slope of the LSV plots exceeds 0.1 mA cm^{-2} V^{-1}) and the current generation (Fig. S10). The more positive the onset potential, the lower the activation overpotential and thus the lower the energy that is required to initiate the reaction. In this case, the onset potential of all Ni-containing electrocatalysts was determined to be rather similar and equal to approximately -0.15 V vs. RHE, which means that all electrocatalysts have a similar active site (most likely Ni-N_X). Furthermore, this value is rather close to the standard reduction potential of CO_2 to CO (i.e. -0.12 V vs. RHE) and signifies that these materials do not require a lot of excess energy input to start the reaction. The metal-free electrocatalysts had a bit more negative onset potential (-0.20 V vs. RHE) and thus require slightly higher energy inputs. With respect to the overall current densities (Fig. S10) and the partial CO current densities (Fig. 7(A)), several observations can be made. First of all, it is clear that the current density (both overall and CO related) increases with the Ni content as expected when the Ni sites are believed to be the predominant active sites. Secondly, the metal-free electrocatalysts seem to result in the largest overall current densities. Unfortunately, once a certain threshold potential (-0.6 V vs. RHE) is reached the obtained current is mainly ascribed to the hydrogen evolution reaction (HER) as also evidenced by the CO partial currents (Fig. 7(A)) and the values for the Faradaic efficiency (Fig. 7(B) and S11, S12 (GC values for Ni-N-AC-B1) and S13 (calibration curves)). This thus means that even though CO can be selectively obtained in the absence of nickel, the presence of nickel is required to achieve higher current densities and thus higher conversions of CO_2, which is important in industrial applications. The Faradaic efficiencies (FE) were further determined to evaluate the selectivity of the different electrocatalysts. The results show that the only formed reduction products are H_2 and CO. Fig. 7(B) and S11, respectively present the CO and H_2 Faradaic efficiencies. All electrocatalysts exhibit a region with >99% selectivity towards CO. For the metal-free electrocatalysts this region is limited to -0.5 to -0.6 V vs. RHE after which the FE_{CO} seriously drops as a consequence of the HER. For the Ni-containing electrocatalysts this region is shifted to more negative values -0.7 to -0.8 V but resulting in higher current densities and thus higher activities. A maximum CO partial current density of -4.5 mA cm^{-2} with a FE_{CO} of 84% was achieved with Ni-N-AC-B1. Ni-N-AC-A, Ni-N-AC-B2 and Ni-

N-AC-B3 all reached lower current densities and Ni-N-AC-C resulted in a much lower FE to CO. Finally, to analyze the kinetic behavior j_{CO}-η curves were constructed to determine the Tafel slope which revealed that the Tafel slope is the lowest for Ni-N-AC-B1 and Ni-N-AC-B3 at 180 mV dec^{-1} and highest for Ni-N-AC-C and N-AC-pure-A at 287 and 360 mV dec^{-1}, respectively, further indicating the superior performance of Ni-N-AC-B1 as a smaller slope indicates faster kinetics (Table S2). Since a Tafel slope of 270 mV dec^{-1} is generally linked with the CO_2 adsorption/CO desorption as rate determining step (RDS), we believe that most of our electrocatalysts will also have this step as their RDS.[24] For Ni-N-AC-B1 the Tafel slope is already smaller, meaning that the kinetics of the adsorption/desorption have increased significantly and will no longer determine the rate. However, a Tafel slope of 180 mV dec^{-1} is still too far from the value of 118 mV dec^{-1}, which is generally found for electrocatalysts with active sites of the type Ni-N_x and have the first electron transfer as the RDS.[24–26,44] In analogy with a recent study by Li *et al.*, where similar Tafel slopes of 180 mV dec^{-1} were obtained, we suggest that the protonation, following on the first electron transfer, of *CO_2 to achieve *COOH is the rate determining step for Ni-N-AC-B1.[26,28] The mechanism for the production of CO from CO_2 on this specific type of Me-N-C type of electrocatalysts has been described previously in the literature and consists of the following steps: (1) CO_2 adsorption; (2) first electron and proton transfer to yield adsorbed COOH; (3) second electron and proton transfer to yield adsorbed CO and release water; and (4) CO desorption to liberate the active site for another reaction.[24,26] In our case, the RDS will be step 1 or step 2 depending on the material under investigation. Based on the above conclusion it is thus clear that the activity increases with the incorporation of Ni and that the Ni-based electrocatalysts decrease in performance from Ni-N-AC-B1 > Ni-N-AC-B2 > Ni-N-AC-B3 > Ni-N-AC-A > Ni-N-AC-C. This order can be rationalized based on the material properties, i.e. degree of graphitization and Ni content and configuration. Based on previous literature data, it was already evidenced that the dominant active site in this kind of electrocatalyst is the Ni-N_X configuration.[4,15,19] This would thus mean that the highest activity should be achieved for the material with the largest fraction of this kind of species, which does seem to be the case for most of the materials. Indeed, Ni-N-AC-B1 has the largest fraction of Ni-N_X species with the exception of Ni-N-AC-C and results in the best performance. The reason why Ni-N-AC-C does not follow this ranking is believed to be caused by the presence of a large fraction of other Ni species: NiO and $Ni(OH)_2$ which are most likely reduced to metallic Ni at increasing overpotentials, and the presence of the latter favors the HER, as known from literature.[9]

To investigate the reproducibility of the electrochemical measurements and the synthesis methods, all experiments were performed at least in duplicate and in some cases a fresh batch of catalyst was prepared. Given the rather small variation in selectivity (Fig. 7B), we could conclude that both our synthesis method and our electrochemical analysis method is quite reproducible.

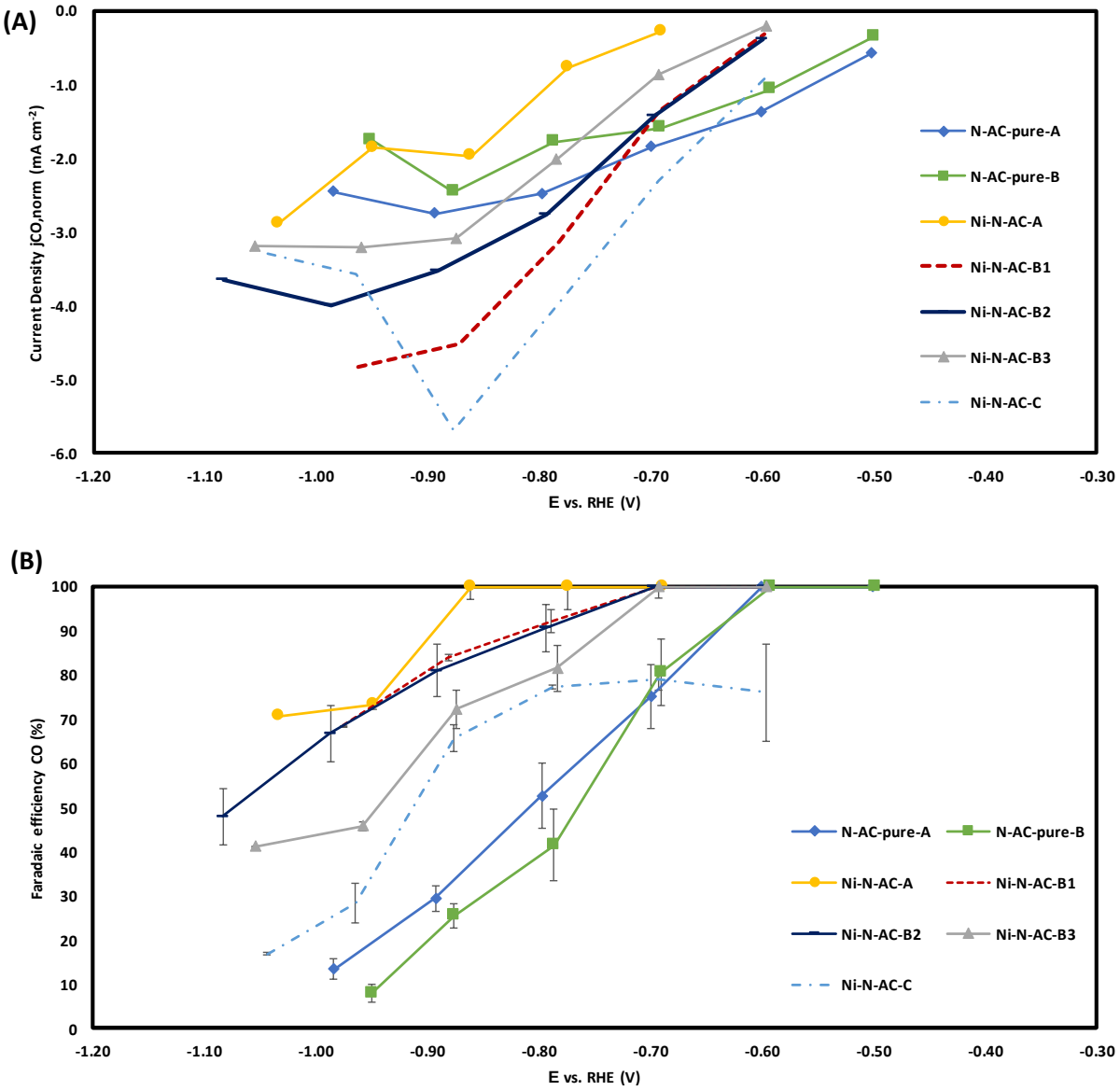

Figure 7. (A) Normalized partial current densities (error was less than 0.1mA.cm^{-2}) to CO and (B) Faradaic efficiencies to CO measured after 25 min of chrono-amperometry experiments performed at set potentials in CO_2-saturated 0.1 M $KHCO_3$ solution.

Notably, the maximum Faradaic efficiency that was achieved with the materials in question is also superior to most of the values that were already reported in literature for similar materials (see Table 3). Furthermore, in most cases they were also achieved at lower overpotentials. To the best of our knowledge, the only exception reported to date is FeMn-N-C, (maximum FE at an overpotential of 0.40 V, i.e. 0.17 V lower than our best materials), yet at a maximum FE of only 80%. In terms of partial CO current densities (mA.cm^{-2}), on the other hand, the materials under investigation are seriously outperformed by the electrocatalysts available in literature, especially when looking at the Ni-containing electrocatalysts (entry 9, 10, 11 & 13). It is important to mention that for entry 10 and 13, the results were achieved using a higher concentration of $KHCO_3$ (0.5 M or even 1 M vs. 0.1 M), partially explaining this big difference in current (*vide infra*). Additionally, for entry 13 carbon paper was used as support providing additional surface area resulting in the increased current densities. To get a better comparison between

the different electrocatalysts and what is described in literature, the values for the current density in terms of current per gram of active site and the turnover frequency (TOF) were also determined (Table 3, last two columns). When taking these data into account it is clear that the prepared materials actually outperform the literature materials both with respect to the activity per active site ($A.g^{-1}$) and with respect to the amount of mmol CO that can be produced per $h.m^2$. Additionally, it also appears that Ni-N-AC-B2 reaches the highest overall performance although generating smaller currents, which is most likely caused by the smaller number of active sites that are available in comparison with Ni-N-AC-B1.

Based on the data available in table 3, several conclusions can thus be drawn. First of all, it is clear that the metal-free electrocatalysts already outperform those prepared in literature using a similar synthesis procedure (e.g. compare entry 1 with entry 3). This is a consequence of the higher surface area here (S_{BET} >700 $m^2.g^{-1}$ compared to S_{BET} < 300 $m^2.g^{-1}$ in literature) and thus the higher number of accessible active sites that go along with such an increase. Secondly, when comparing entry 14 with entry 5, it is clear that although the synthesis method is identical, improved performance for the reduction of CO_2 to CO can be achieved by using Ni as metal species instead of a combination of Fe and Mn.[15] Finally, while similar Ni-containing electrocatalysts were already reported in literature with a better overall performance, it is believed that electrocatalysts can be prepared using the proposed synthesis method with a better overall performance (mainly higher current densities) than those already available in literature simply by increasing the number of active sites. Indeed, when looking at the currents per active site and the turnover frequencies, it is clear that the as-prepared electrocatalysts reach a better intrinsic performance per individual active site. This highlights an additional advantage of the applied synthesis method as it is very versatile and can thus be easily tuned to include a higher number of active sites. Furthermore, it is based on cheap and easily accessible materials (vs. bypiridine which is used for the synthesis of Ni-N-C (entry 9)[4]) and can also be easily modified to include other metals and as such alter the selectivity to for example produce formic acid (Sn or Pb as metal) or methane (Cu as metal).[45]

Table 3. Electrocatalytic performance of various non-noble metal-containing N-doped carbons for the reduction of CO_2 to CO.

Entry	Sample	Max. FE_{CO} (%)	Overpotential η (V)	Max. J_{CO} ($mA.cm^{-2}$)	Max. J_{CO} ($A.g^{-1}$ active site)[a]	TOF ($mmol.h^{-1}.m^{-2}$) @ -0.7 V vs. RHE
1	N-AC-pure-A	>99%	0.47	-2.8	-140	0.5
2	N-AC-pure-B	>99%	0.47	-2.5	-43	0.3
3	N-C [15]	70%	0.49	-0.6	-8	n.d.[c]
4	Ni-N-AC-A	>99%	0.57	-2.9	n.d.[c]	n.d.[c]
5	Ni-N-AC-B1	>99%	0.57	-4.0	-613	16.1
6	Ni-N-AC-B2	>99%	0.57	-3.2	-690	26.8
7	Ni-N-AC-B3	>99%	0.57	-4.2	-575	22.5
8	Ni-N-AC-C	79%	0.57	-1.4	-52	1.4
9	Ni-N-C [4]	85%	0.67	-17	-590	n.d.[c]
10	$Ni-N_4-C$ [3b]	>99%	0.69	-29	n.d.[c]	20
11	Ni-N-C [20]	80%	0.69	-12	-630	n.d.[c]
12	Ni-N-C [24]	93%	0.56	-3.9	n.d.[c]	n.d.[c]
13	Ni-N-C [27]	95%	0.90	-72	-662	n.d.[c]
14	FeMn-N-C [15]	80%	0.40	-5.5	-175	18

[a]Calculated based on the maximum partial current density to CO and taking into account the catalyst loading and the weight percentage of active sites (N for N-AC-pure and $Ni-N_x$ for Ni-N-AC).

[b]Important note: measurements were performed in 0.5 M $KHCO_3$ instead of 0.1 M $KHCO_3$ as was the case in this study.

[c]Not determined because of the absence of a Ni XPS signal or the lack of data in the literature publications.

Based on the values obtained for the overall performance (FE_{CO}, overpotential and J_{CO} in $mA.cm^{-2}$), Ni-N-AC-B1 was selected as the most promising candidate for the electrochemical reduction of CO_2 to CO and was further investigated to unravel the impact of catalyst loading and $KHCO_3$ concentration on CO_2 reduction (see Fig. S14). First of all, Ni-N-AC-B1 was evaluated in a CO_2-saturated 0.5 M $KHCO_3$ solution. We observed that while the values of FE_{CO} did not change significantly, the maximum partial CO current density increased 5-fold, , resulting in a maximum value of -19 $mA.cm^{-2}$, bringing it closer to the reported literature data (entry 10, which was measured in 0.5M $KHCO_3$). As the type of active sites and their relative contribution did not change, it is straightforward to understand that also the FE did not change. The increase in current density is most likely ascribed to the increased conductivity (and thus decreased charge transfer resistance) and the increased pH (7.3 compared to 6.8,and thus lower $[H^+]$) both promoting faster reaction kinetics and thus higher currents.[12] Another explanation can be found in the role of bicarbonate in the CO_2 reduction. Indeed, since a recent isotopic labeling study[46] indicated that the bicarbonate anion is the primary source of CO_2 at the active surface, it is straightforward that the current should increase with the bicarbonate concentration. Secondly, the loading of the electrocatalyst on the glassy carbon disk was decreased from 785 $\mu g.cm^{-2}$ to 200 $\mu g.cm^{-2}$ (in accordance with [3]) while maintaining the electrolyte concentration at 0.5 M. From Fig. S14, it can be deduced that this almost 4-fold decrease in electrocatalyst loading resulted in a decrease in performance (i.e. current density) to the original values which were obtained using the 0.1 M $KHCO_3$ solution. This is a natural consequence of the decrease in the number of available active sites for CO_2 reduction. Finally, it appears that the impact of the catalyst loading on the current density is larger than that

of the electrolyte concentration. Indeed, the effect of 4-fold decrease in loading results in the same decrease in activity as a 5-fold decrease in $KHCO_3$ concentration.

We went on to evaluate the stability of Ni-N-AC-B1 by means of long-term chrono-amperometry experiments at -0.8 V vs. RHE in 0.5 M $KHCO_3$ (Fig. 8). These tests revealed both a decrease in current density (approx. 25% over 24h) and a decrease in Faradaic efficiency towards CO over time (approx. 13% decrease). Both are more likely a consequence of the employed cell configuration and stationary electrolyte rather than degradation of the electrocatalyst (see also flow-cell experiments where FE and current density remain quasi constant). Indeed, since a stationary electrolyte is used, it is highly likely that the thickness of the diffusion layer increases over the course of time, resulting in a serious reduction of the available CO_2 at the surface.[47] This in turn will result in a higher selectivity towards the hydrogen evolution reaction and thus a decrease in FE to CO.

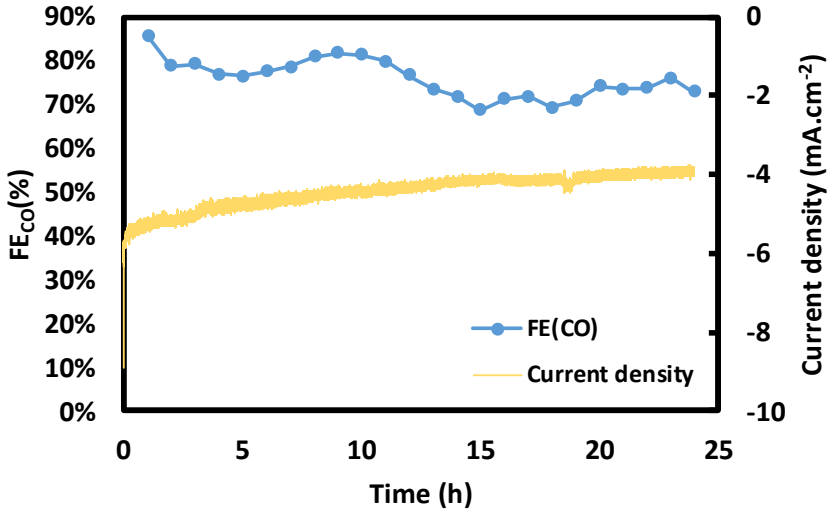

Figure 8. Chrono-amperometry results for Ni-N-AC-B1 in CO_2-saturated 0.5 M $KHCO_3$ at -0.8 V vs. RHE and the corresponding change in FE_{CO}.

3.2.2 Flow cell

In a last set of experiments, Ni-N-AC-B1 was also evaluated for the CO_2 reduction in an in-house designed gas-diffusion electrode-based flow-cell to investigate its applicability in an actual electrolyzer (see experimental section for more details regarding the setup).

Based on the batch-cell measurements, three potentials (-0.7; -0.8 & -0.9 V vs. RHE) were selected at which the performance of Ni-N-AC-B1 was evaluated in flow. Based on these tests (Fig. 9) it could be concluded that this type of electrocatalysts performs at least equally well under flow conditions as it did in a H-cell. Indeed, at all three potentials an almost complete selectivity (>95% FE) to CO was achieved. Additionally, slightly improved current densities were achieved in flow which is most likely caused by the increased CO_2 concentration at the gas-liquid interface and improved mass transfer of both reagents and products to and from the active sites.[48]

In order to quantify the productivity of the employed Ni-N-C electrocatalyst in this particular setup, we calculated the amount of g CO produced per hour and per square meter. The productivity went up from 54 to 113 g $CO.h^{-1}.m^{-2}$ when the applied overpotential increased from -0.7 to -0.9 V vs. RHE. In comparison with the literature on CO_2 reduction in flow-cells this value is on the low side with respect to the values achieved using a typical CO generating catalyst like silver, which go from 110 up to 1000 $g.h^{-1}m^{-2}$ in aqueous $KHCO_3$. It goes

without saying that this increase in productivity goes at the cost of a serious increase in electrocatalyst cost, which is obviously much higher for silver than for our Ni-based electrocatalysts.[12,49,50] When our results are compared with other reports available on similar electrocatalysts (i.e. Ni-N_x-based), productivities from 250 to 950 g $CO.h^{-1}.m^{-2}$ could be found, which means that also here there is room for improvement. However, in our opinion this should be achievable by modifying the synthesis method to include a larger number of active Ni-N_x sites, given their high intrinsic activity (see table 3).[20,21,25] Indeed, the positive impact of increasing the number of Ni-N_x sites on the activity was already evidenced here when comparing e.g. Ni-N-AC-A with Ni-N-AC-B1. In future work, different routes to increase the number of active N sites or simply improve their accessibility will be undertaken to prove this statement. Some possibilities include, altering the N source to e.g. melamine, which would allow us to incorporate more N and thus more Ni or starting with a more open (mesoporous) support like ordered mesoporous carbons which will increase accessibility, etc.. But this falls outside the scope of the current work.

Unfortunately, comparing the maximum productivity for Ni-N-AC-B1 of 1 ton per year and per square meter with the current annual global production of CO, which amounts to approximately 2 million tons per year, it is clear that the productivity has to be further increased for this technique to replace current technologies.[51]

The reported productivity was obtained at a cell voltage of 3V, which is comparable to data available in literature.[48,52] Using this value of the cell voltage the energy efficiency was calculated according to the following formula (Eq.2)[52]:

$$\varepsilon = \frac{FE.E_k^0}{E_{cell}} \qquad \text{(Eq. 2)}$$

where E_k^0 is the equilibrium cell potential for the product under investigation (i.e. -1.33 V for CO). We report a value of 42% which is comparable to those reported earlier using more expensive Ag catalysts.[12,49,50]

All of the above lead to the same conclusion that the Ni-N-C electrocatalysts synthesized in this work are promising candidates for the electrochemical reduction of CO_2 to CO and could bring this technique closer to its industrial application given that the productivity can and should be further improved by increasing the number of available active sites.

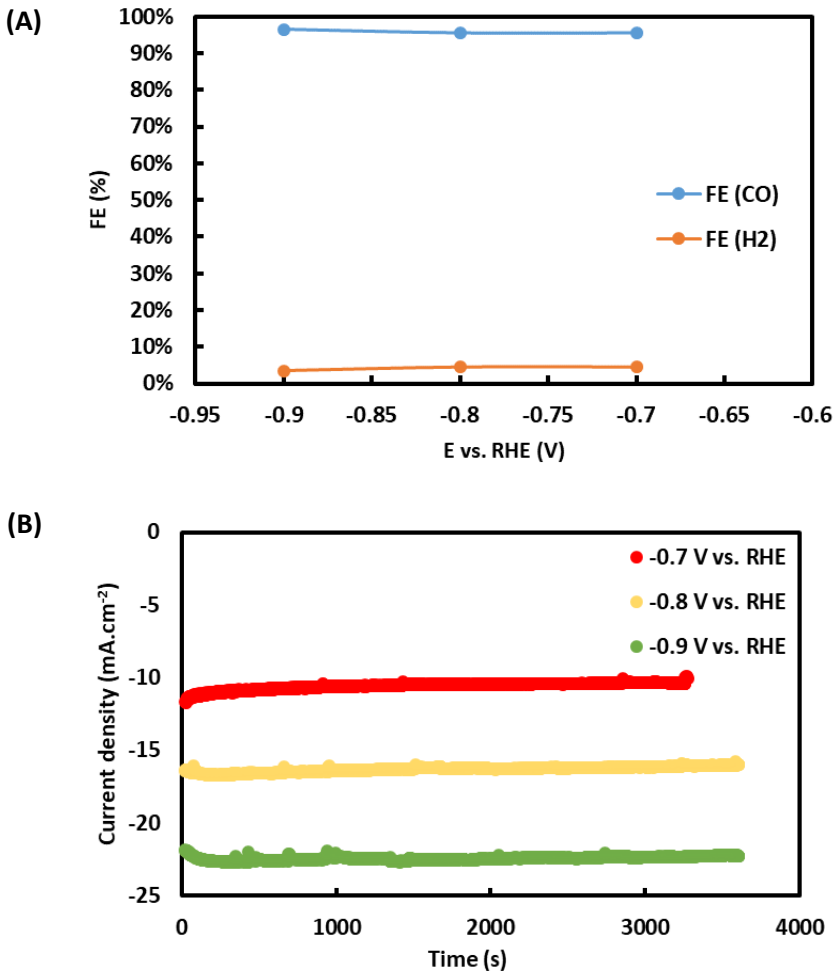

Figure 9. (A) Average FE to CO and H_2 after one hour chrono-amperometry in CO_2-saturated 0.5 M $KHCO_3$ and (B) corresponding chrono-amperometry curves.

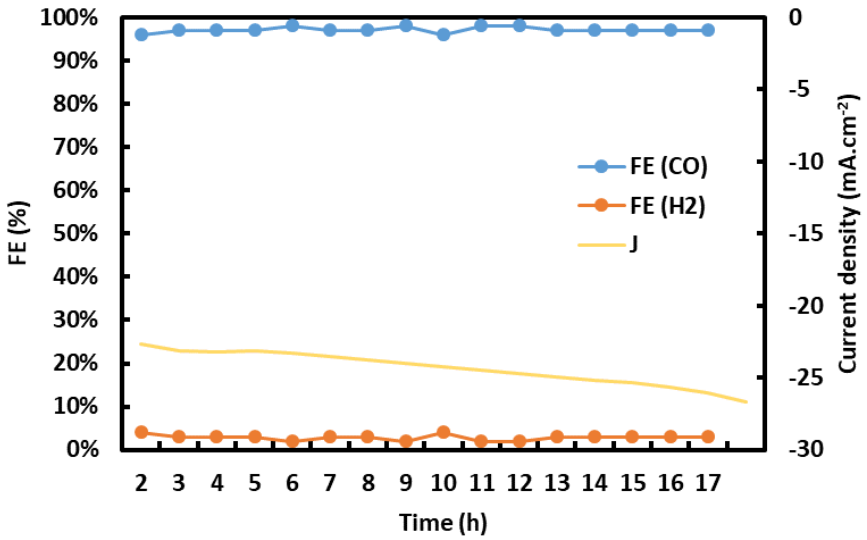

Figure 10. Chrono-amperometry measurement in the flow-cell of Ni-N-AC-B1 at a constant potential of -0.9 V vs. RHE and corresponding values of Faradaic efficiency.

Next, the stability of Ni-N-AC-B1 was also evaluated in the flow-cell configuration for 16h (Fig. 10). It is clear that both activity and selectivity remain stable over the length of the experiment, highlighting the possibilities of this type of electrocatalyst for larger scale application. There is even an increase in current density over the duration of the experiment, which is tentatively ascribed to a decrease in the Ohmic resistance as a consequence of the transport of potassium ions from anolyte to catholyte through the Nafion® membrane.

Afterwards, the impact of the composition of the cell (electrolytes, membrane, anode) on the overall reaction performance was investigated. A comparison was made at different current densities (from 25 to 100 $mA.cm^{-2}$) in terms of resulting selectivity towards CO and the required cell potential. To avoid the impact of the potential drift of the reference electrode upon changing the cell configuration, we have chosen here to work at constant current instead of constant potential and thus utilized a 2-electrode configuration. From an industrial perspective this is also more interesting as the cell potential gives more important information than the working electrode potential alone, which does not allow to calculate the energy requirements of the resulting setup. Several conclusion can be drawn from Figure 11. First of all, it is clear that when utilizing IrO_2 as anode instead of Pt, a big improvement can be seen in terms of cell potential and also to a minor extent in selectivity to CO, especially at higher current densities. It is thus clear that the oxygen evolution reaction occurs at lower overpotential when utilizing IrO_2 under these conditions. Secondly, to avoid electrolyte cross-over between both compartments, it was investigated if the anode reaction would perform as good when utilizing a 1 M $KHCO_3$ solution instead of 2 M KOH, unfortunately, this was not the case as an increase in cell potential could be observed. Next, given the fact that the use of 2 M KOH is beneficial for the oxygen evolution reaction, it can be expected that Nafion®, a cation-exchange membrane, is not the most suitable membrane for efficient operation. For this reason, two anion-exchange membranes, Fumatech® and Selemion®, were used as alternative and although they resulted in a small increase in cell potential, they did result in enhanced selectivities to CO, especially Fumatech which lead to an increase of >20% in FE_{CO} at 100 $mA.cm^{-2}$. We believe this is due to the fact that it allows a fast transport of the hydroxyl ions from the anode where they are generated to the cathode where they are used to reduce CO_2. When comparing the results obtained with Selemion® and Fumatech® it is clear that Fumatech® is the better option both resulting in lower cell potentials and higher selectivities to CO, which we ascribe to the fact that Fumatech® is thinner, allowing faster hydroxyl cross-over and has a slightly smaller resistance, both resulting in a decreased Ohmic resistance and thus lowered cell potential. Finally, by increasing the catholyte concentration from 0.5 to 1 M $KHCO_3$ utilizing Selemion® as a membrane, yielded a lower cell potential and an increase in selectivity. The former is related with an increased conductivity, which results in a decrease in the cathode overpotential. The latter is a consequence of the increase in pH with the increasing $KHCO_3$ concentration. Indeed, it is known from literature that an increase in pH is known to result in slower hydrogen evolution reaction kinetics and will thus favor the production of CO over H_2.[53]

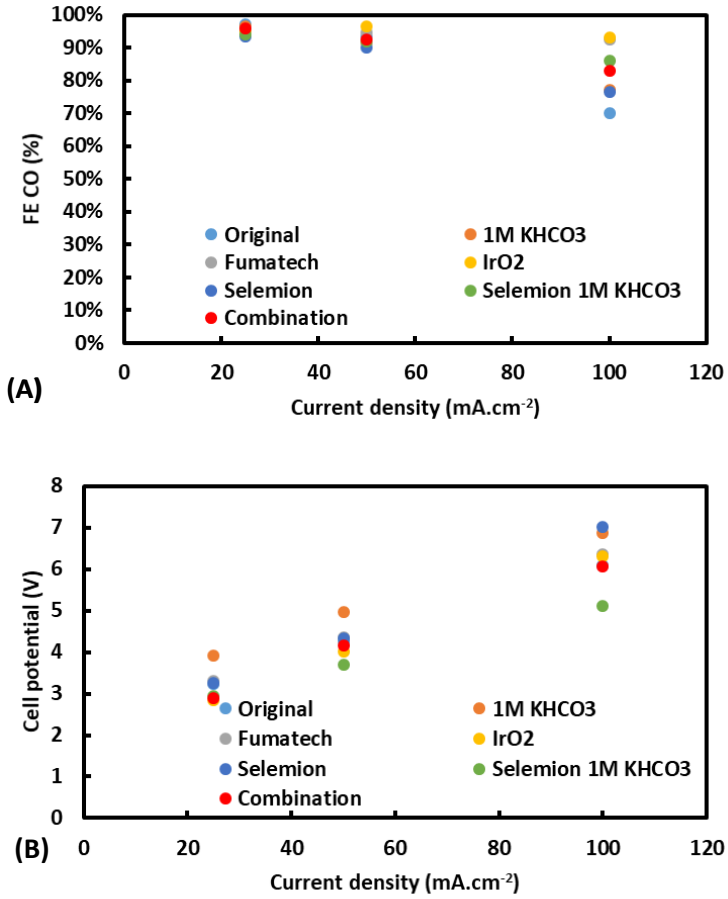

Figure 11. Impact of cell configuration on the overall performance of Ni-N-AC-B1 in a flow cell (A) Faradaic efficiency and (B) cell potential.

For further optimization, it was attempted to combine the best option for all three parameters (anode, membrane, and electrolyte composition) and investigate its impact on cell potential and selectivity. Based on the results the following configuration was chosen: (1) IrO_2 as anode; (2) Fumatech® as membrane and (3) 1 M $KHCO_3$ and 2M KOH as catholyte and anolyte, respectively, and the same tests were repeated. Unfortunately, while this did seem to yield the best results at low current density, its performance quickly decreased at higher current densities (Fig.11, combination entry). It is believed that this quick decrease in performance has to do with a degradation of the IrO_2 anode catalyst. Indeed, when comparing the increase in cell potential at -50 $mA.cm^{-2}$ when utilizing IrO_2 as anode to the case where Pt was used, a much faster decay is observed (Fig. S15). For this reason, Pt will be utilized as anode in the remaining experiments.

In conclusion, these experiments thus clearly show the importance of optimizing the cell configuration for this kind of electrocatalyst as they result in a significant improvement of FE to CO (>15%) and a decrease in the required cell potential (by 0.3 to 1.0 V compared to the original configuration), especially at larger current densities.

Finally, the possibility to utilize this type of electrocatalyst at higher current densities (50 $mA.cm^{-2}$) for extended durations was investigated utilizing the optimized cell configuration (anode: Pt, membrane: Fumatech® and catholyte and anolyte: 1 M $KHCO_3$ and 2 M KOH, respectively) as industrial applications require larger and stable productivities and thus imply larger current densities (Fig. 12). At the beginning of the experiment, it is

clear that high FE's to CO could be achieved. In terms of productivity a value of 250 g $CO.h^{-1}m^{-2}$ was achieved, which approaches some of the values obtained in literature with the Ag-based electrocatalysts, and could be further improved by further increasing the applied current density (i.e. 480 g $CO.h^{-1}.m^{-2}$ was achieved at 100 $mA.cm^{-2}$).[12,49,50] Unfortunately, the values of FE to CO slightly decreased over time, until an FE to CO of about 80% was reached after 24h, correlating with a productivity of 210 g $CO.h^{-1}m^{-2}$ (or FE of 80%). Also a clear increase in cell potential could be observed. While the former is most likely linked with stability issues of the cathode catalyst, the latter is both a consequence of electrode and electrolyte degradation. Indeed, after 21h the electrolyte was refreshed, which resulted in an immediate decrease in cell potential as visualized by the sharp peak in Fig. 12. To conclude, further research on the catalyst's stability under optimized flow process conditions is required in order to advance commercialization of this technology.

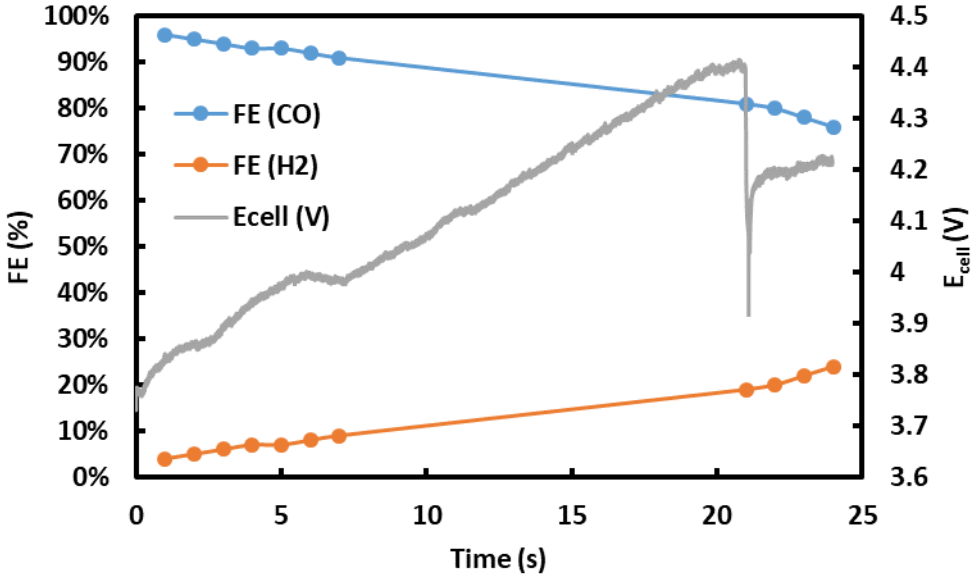

Figure 12. Chrono-potentiometry measurement at a constant current density of -50 $mA.cm^{-2}$ and corresponding values of Faradaic efficiency and cell voltage. The following flow cell configuration was used: ion-exchange membrane: Fumatech®, anode catalyst: Pt and catholyte and anolyte composition: 1 M $KHCO_3$ and 2 M KOH, respectively.

4. Conclusions

This study introduced Ni-containing N-doped carbons as promising candidates for the electrochemical reduction of CO_2 to CO, prepared through a cheap, versatile and easily up-scalable method. The activity of the synthesized electrocatalysts was ranked based on their overpotential and current density, whereas the selectivity was estimated by means of gas chromatography. The nature of the metal center, the N configuration and their final content proved to strongly influence the electrocatalytic performance, especially in terms of current density and selectivity to CO. Ni-N-AC-B1 synthesized with a high relative amount of nitrogen and nickel, was identified as the most promising candidate for this reaction based on its partial CO current ($4.2mA.cm^{-2}$), its overpotential (0.57 V) and its Faradaic efficiency to CO (> 99%). This resulted in unprecedented values for the current density per g active sites (690 $A.g^{-1}$ active sites). Based on a thorough physicochemical characterization, it could be concluded that nickel in a configuration bound with nitrogen ($Ni\text{-}N_x$) is the major specie contributing to a good performance for the electrochemical CO_2 reduction to CO. The presence of metallic nickel on the other hand, seemed to promote the

competing hydrogen evolution reaction and resulted in larger values of Faradaic efficiency towards H_2 as was the case for Ni-N-AC-C. Finally, Ni-N-AC-B1 was also put to the test in an actual electrolyzer and similar activities and selectivities were achieved, further evidencing its potential to produce CO electrochemically from CO_2 on a larger scale. Additionally, the flow-cell configuration was optimized in an attempt to further improve performance. This investigation resulted in substantial improvements in terms of cell potential and selectivity to CO, especially at large current densities. The following combination of parameters was found as optimal: Pt as anode, Fumatech® as membrane and 1 M $KHCO_3$ and 2 M KOH as catholyte and anolyte, respectively. In our opinion, this work thus clearly offers a unique combination of electrocatalyst development and reactor optimization for this specific type of electrocatalyst, indicating its importance as an essential first step towards up-scaling and ultimately industrial application of this technique.

Conflicts of interest

There are no conflicts of interest to declare.

Acknowledgements

The authors acknowledge sponsoring from the research foundation of Flanders (FWO) in the frame of a post-doctoral grant (12Y3919N – ND). J. Hereijgers was supported through a postdoctoral fellowship (28761) of the Research Foundation – Flanders (FWO). This project was co-funded by the Interreg 2 Seas-Program 2014-2020, co-financed by the European Fund for Regional Development in the frame of subsidiary contract nr. 2S03-019. This work was further performed in the framework of the Catalisti cluster SBO project CO2PERATE ("All renewable CCU based on formic acid integrated in an industrial microgrid"), with the financial support of VLAIO (Flemish Agency for Innovation and Entrepreneurship). This project finally received funding from the European Research Council (ERC Consolidator Grant 815128, REALNANO). We thank Karen Leyssens for helping with the N_2 physisorption measurements and Kitty Baert (VUB) for analyzing the samples with XPS and Raman.

References

1 A. Vasileff, Y. Zheng and S. Z. Qiao, *Adv. Energy Mater.*, 2017, **7**, 1–21.

2 S. Hernández, M. A. Farkhondehfal, F. Sastre, M. Makkee, G. Saracco and N. Russo, *Green Chem.*, 2017, **19**, 2326–2346.

3 X. Li, W. Bi, M. Chen, Y. Sun, H. Ju, W. Yan, J. Zhu, X. Wu, W. Chu, C. Wu and Y. Xie, *J. Am. Chem. Soc.*, 2017, **139**, 14889–14892.

4 W. Ju, A. Bagger, G. P. Hao, A. S. Varela, I. Sinev, V. Bon, B. Roldan Cuenya, S. Kaskel, J. Rossmeisl and P. Strasser, *Nat. Commun.*, 2018, **8**, 944–953.

5 R. Kortlever, J. Shen, K. J. P. Schouten, F. Calle-Vallejo and M. T. M. Koper, *J. Phys. Chem. Lett.*, 2015, **6**, 4073–4082.

6 M. S. Xie, B. Y. Xia, Y. Li, Y. Yan, Y. Yang, Q. Sun, S. H. Chan, A. Fisher and X. Wang, *Energy Environ. Sci.*, 2016, **9**, 1687–1695.

7 M. Gattrell, N. Gupta and A. Co, *J. Electroanal. Chem.*, 2006, **594**, 1–19.

8 Y. Zhao, J. Liang, C. Wang, J. Ma and G. G. Wallace, *Adv. Energy Mater.*, 2018, **8**, 1–9.

9 J. Qiao, Y. Liu, F. Hong and J. Zhang, *Chem. Soc. Rev.*, 2014, **43**, 631–75.

10 Y. Hori, H. Konishi, T. Futamura, A. Murata, O. Koga, H. Sakurai and K. Oguma, *Electrochim. Acta*, 2005, **50**, 5354–5369.

11 Y. Hori, A. Murata and R. Takahashi, *J. Chem. Soc., Faraday Trans. 1*, 1989, **85**, 2309–2326.

12 S. Verma, X. Lu, S. Ma, R. I. Masel and P. J. A. Kenis, *Phys. Chem. Chem. Phys.*, 2016, **18**, 7075–7084.

13 A. S. Varela, W. Ju, T. Reier and P. Strasser, *ACS Catal.*, 2016, **6**, 2136–2144.

14 K. Manthiram, B. J. Beberwyck and A. P. Alivisatos, *J. Am. Chem. Soc.*, 2014, **136**, 13319–13325.

15 A. S. Varela, N. Ranjbar Sahraie, J. Steinberg, W. Ju, H. S. Oh and P. Strasser, *Angew. Chemie - Int. Ed.*, 2015, **54**, 10758–10762.

16 J. H. Kim, H. Woo, S. W. Yun, H. W. Jung, S. Back, Y. Jung and Y. T. Kim, *Appl. Catal. B Environ.*, 2017, **213**, 211–215.

17 E. R. Cave, J. H. Montoya, K. P. Kuhl, D. N. Abram, T. Hatsukade, C. Shi, C. Hahn, J. K. Nørskov and T. F. Jaramillo, *Phys. Chem. Chem. Phys.*, 2017, **19**, 15856–15863.

18 M. R. Singh, Y. Kwon, Y. Lum, J. W. Ager and A. T. Bell, *J. Am. Chem. Soc.*, 2016, **138**, 13006–13012.

19 X. Li, W. Bi, M. Chen, Y. Sun, H. Ju, W. Yan, J. Zhu, X. Wu, W. Chu, C. Wu and Y. Xie, *J Am Chem Soc*, 2017, **139**, 14889–14892.

20 T. Möller, W. Ju, A. Bagger, X. Wang, F. Luo, T. Ngo Thanh, A. S. Varela, J. Rossmeisl and P. Strasser, *Energy Environ. Sci.*, 2019, **12**, 640–647.

21 K. Jiang, S. Siahrostami, T. Zheng, Y. Hu, S. Hwang, E. Stavitski, Y. Peng, J. Dynes, M. Gangisetty, D. Su, K. Attenkofer and H. Wang, *Energy Environ. Sci.*, 2018, **11**, 893–903.

22 M. Jia, C. Choi, T. S. Wu, C. Ma, P. Kang, H. Tao, Q. Fan, S. Hong, S. Liu, Y. L. Soo, Y. Jung, J. Qiu and Z. Sun, *Chem. Sci.*, 2018, **9**, 8775–8780.

23 D. Tan, C. Cui, J. Shi, Z. Luo, B. Zhang, X. Tan, B. Han, L. Zheng, J. Zhang and J. Zhang, *Nano Res.*, 2019, **12**, 1167–1172.

24 X. M. Hu, H. H. Hval, E. T. Bjerglund, K. J. Dalgaard, M. R. Madsen, M. M. Pohl, E. Welter, P. Lamagni, K. B. Buhl, M. Bremholm, M. Beller, S. U. Pedersen, T. Skrydstrup and K. Daasbjerg, *ACS Catal.*, 2018, **8**, 6255–6264.

25 T. Zheng, K. Jiang, N. Ta, Y. Hu, J. Zeng, J. Liu and H. Wang, *Joule*, 2019, **3**, 265–278.

26 F. Pan, W. Deng, C. Justiniano and Y. Li, *Appl. Catal. B Environ.*, 2018, **226**, 463–472.

27 C. Yan, H. Li, Y. Ye, H. Wu, F. Cai, R. Si, J. Xiao, S. Miao, S. Xie, F. Yang, Y. Li, G. Wang and X. Bao, *Energy Environ. Sci.*, 2018, **11**, 1204–1210.

28 M. Zhang, T.-S. Wu, S. Hong, Q. Fan, Y.-L. Soo, J. Masa, J. Qiu and Z. Sun, *ACS Sustain. Chem. Eng.*, 2019, **7**, 15030–15035.

29 N. Daems, J. Wouters, K. Baert, C. Poleunis, A. Delcorte, A. Hubin, I. F. J. Vankelecom and P. P. Pescarmona, *Appl. Catal. B Environ.*, 2018, **226**, 509–522.

30 N. Daems, X. Sheng, Y. Alvarez-Gallego, I. F. J. Vankelecom and P. P. Pescarmona, *Green Chem.*, 2016, **18**, 1547–1559.

31 G. Wu, K. L. More, C. M. Johnston and P. Zelenay, *Science*, 2011, **332**, 443–447.

32 M. K. Van Der Lee, A. Van Jos Dillen, J. H. Bitter and K. P. De Jong, *J. Am. Chem. Soc.*, 2005, **127**, 13573–13582.

33 B. De Mot, J. Hereijgers, M. Duarte and T. Breugelmans, *Chem. Eng. J.*, 2019, **378**, 122224.

34 B. Endrődi, E. Kecsenovity, A. Samu, F. Darvas, R. V. Jones, V. Török, A. Danyi and C. Janáky, *ACS Energy Lett.*, 2019, **4**, 1770–1777.

35 I. Herrmann, U. I. Kramm, J. Radnik, S. Fiechter and P. Bogdanoff, *J. Electrochem. Soc.*, 2009, **156**, B1283–B1292.

36 M. El-Kemary, N. Nagy and I. El-Mehasseb, *Mater. Sci. Semicond. Process.*, 2013, **16**, 1747–1752.

37 H. L. Chen, Y. M. Lu and W. S. Hwang, *Surf. Coatings Technol.*, 2005, **198**, 138–142.

38 J. Yan, Z. Fan, W. Sun, G. Ning, T. Wei, Q. Zhang, R. Zhang, L. Zhi and F. Wei, *Adv. Funct. Mater.*, 2012, **22**, 2632–2641.

39 N. Daems, X. Sheng, I. F. J. Vankelecom and P. P. Pescarmona, *J. Mater. Chem. A*, 2014, **2**, 4085–4110.

40 G. Wu, C. M. Johnston, N. H. Mack, K. Artyushkova, M. Ferrandon, M. Nelson, J. S. Lezama-Pacheco, S. D. Conradson, K. L. More, D. J. Myers and P. Zelenay, *J. Mater. Chem.*, 2011, **21**, 11392–11405.

41 K. T. Lee, X. Ji, M. Rault and L. F. Nazar, *Angew. Chemie - Int. Ed.*, 2009, **48**, 5661–5665.

42 H. W. Nesbitt, D. Legrand and G. M. Bancroft, *Phys. Chem. Miner.*, 2000, **27**, 357–366.

43 M. C. Biesinger, B. P. Payne, A. P. Grosvenor, L. W. M. Lau, A. R. Gerson and R. S. C. Smart, *Appl. Surf. Sci.*, 2011, **257**, 2717–2730.

44 P. Lu, Y. Yang, J. Yao, M. Wang, S. Dipazir and M. Yuan, *Appl. Catal. B Environ.*, 2019, **241**, 113–119.

45 R. J. Lim, M. Xie, M. A. Sk, J. M. Lee, A. Fisher, X. Wang and K. H. Lim, *Catal. Today*, 2014, **233**, 169–180.

46 D. Hursán and C. Janáky, *ACS Energy Lett.*, 2018, **3**, 722–723.

47 E. L. Clark, J. Resasco, A. Landers, J. Lin, L. Chung, A. Walton, C. Hahn, T. F. Jaramillo and A. T. Bell, *ACS Catal.*, 2018, **8**, 6560–6570.

48 B. Endrődi, G. Bencsik, F. Darvas, R. Jones, K. Rajeshwar and C. Janáky, *Prog. Energy Combust. Sci.*, 2017, **62**, 133–154.

49 H. R. Q. Jhong, F. R. Brushett and P. J. A. Kenis, *Adv. Energy Mater.*, 2013, **3**, 589–599.

50 S. Ma, R. Luo, J. I. Gold, A. Z. Yu, B. Kim and P. J. A. Kenis, *J. Mater. Chem. A*, 2016, **4**, 8573–8578.

51 D. M. Weekes, D. A. Salvatore, A. Reyes, A. Huang and C. P. Berlinguette, *Acc. Chem. Res.*, 2018, **51**, 910–918.

52 H. R. M. Jhong, S. Ma and P. J. Kenis, *Curr. Opin. Chem. Eng.*, 2013, **2**, 191–199.

53 M. R. Singh, E. L. Clark and A. T. Bell, *Phys. Chem. Chem. Phys.*, 2015, **17**, 18924–18936.